Comparative Analysis of Symmetrical-Component Extraction Methods for IEEE 2800-2022-Compliant Negative-Sequence Regulation in VSM-Based Grid-Forming Inverters

Elochukwu Ihekerem

***Abstract*—This paper compares four extraction methods behind an identical interface in a full-order virtual synchronous machine (VSM) grid-forming inverter: the dual second-order generalized integrator with frequency-locked loop (DSOGI-FLL), delayed signal cancellation (DSC), the extended Kalman filter (EKF) and a super-twisting sliding-mode observer (ST-SMO). Simulations cover short-circuit ratios (SCR) of 1.5, 3 and 5, four fault types and three fault profiles at a converged step of 50 μs, and are checked against an analytic truth, a negative-sequence reference reconstructed offline, and a step-size study. DSOGI-FLL has the smallest estimation error (median angle error 1.0° against 3.3°, 5.2° and 14° for the EKF, DSC and ST-SMO) and the lowest output ripple (median 0.003 pu against 0.016 pu for DSC). Recovery time (median spread 0.01 s) and rotor-angle deviation (at most 2°) are set by the VSM, the fault type and the SCR and not by the extractor. The ST-SMO injection loop oscillates after fault clearing at the gain at which the other methods are stable, so it is run at a lower gain with a nearly inactive injection. Compliance to the IEEE Standard 2800-2022 is assessed on the realized current, because the commanded lead does not determine it.**

***Index Terms*—Grid-forming control, fault ride-through, symmetrical component extraction, virtual synchronous machine, IEEE 2800-2022, negative-sequence current regulation.**

I. Introduction

IEEE Standard 2800-2022 sets uniform requirements for the interconnection of inverter-based resources (IBRs), including ride-through, dynamic voltage support and negative-sequence current injection. Clause 7 requires IBRs to generate both positive- and negative-sequence currents during unbalanced faults, with the negative-sequence current leading the negative-sequence voltage by 90°–100° for full-converter IBRs [1]. The standard does not prescribe how the current references are generated, and the choice of sequence-estimation method is left to the designer.

This matters most for grid-forming (GFM) inverters, which are expected to hold a balanced internal voltage during asymmetrical faults, so the resulting unbalanced current has a negative-sequence component that must be regulated and any error in the estimated sequence components enters the commanded current directly.

E. Ihekerem is a graduate of the Department of Electrical and Electronics Engineering, Landmark University, Omu-Aran, Nigeria (e-mail: ihekerem.elochukwu@lmu.edu.ng; ORCID: 0009-0002-7745-7562).

This is an independent study. It is not affiliated with or endorsed by the IEEE, and it offers no official interpretation of IEEE Std 2800-2022.

November 4, 2026.

Recent work addresses the control side. Nasr and Hooshyar enable GFM IBRs to absorb negative-sequence reactive current while regulating positive-sequence voltage, with an adaptive virtual-impedance current limit [2]. Together with reviews of overcurrent limiting [3] and of GFM control [4], this suggests that a general framework for 2800-compliant GFM control is sparse. What remains open is how the extraction methods compare in the closed loop of a full GFM inverter against the standard's requirements. Zhao *et al.* compare DSC, the dual second-order generalized integrator and the decoupled double synchronous reference frame and show that the choice affects GFM fault dynamics once the converter is current-limited [5], but extraction is there as a secondary element, EKF and ST-SMO are not considered, and no SCR sweep or standard-specific framing is used. Awal *et al.* evaluate five time-domain extraction methods for GFM converters on transient response time, accuracy and implementation [6], and give a small-signal model of sequence-decomposed GFM control with which they compare a filter-based and a delay-based method, finding that the filter-based method limits the achievable current-control bandwidth [7]. The small-signal study is linearized, covers one method from each group, and does not compare fault recovery across methods.

This paper compares DSOGI-FLL, DSC, the EKF and ST-SMO in a full-order VSM-based GFM inverter. Each method is an interchangeable subsystem behind one extraction interface, so the rest of the architecture is identical. One structural difference, however, cannot be circumvented. DSOGI-FLL and the EKF estimate the grid frequency online, whereas DSC and ST-SMO assume the nominal frequency, so differences between methods reflect each algorithm as a whole.

The contributions are as follows. Compliance with the 90°–100° lead requirement is assessed on the *realized* converter current, reconstructed from raw plant signals, and not on the commanded reference, which was found not to determine the realized lead. The extraction-induced regulation error is measured against an offline ground truth that is independent of all four estimators. Ripple, rotor-angle deviation and active-power recovery are compared at SCR of 1.5, 3 and 5 [8], and temporary faults cleared after about 100 ms (primary protection) and 350 ms (breaker-failure backup) allow recovery to be measured against the numeric restoration requirement of the standard. These results are preceded by a validation program (Section IV). SCR $=$ 10 was also simulated, but the base

VSM oscillates there with no fault applied, so it is reported as a limitation (Section V-A) and not as a comparison point. No comparison with grid-following converters is made.

II. System Model

The system is a GFM inverter controlled as a full-order VSM, connected through an LCL filter and a transformer to a grid of variable strength, represented by a series RL impedance set by the SCR. Fig. 1 shows the power circuit and the control architecture: measurement, power control (the VSM), the extraction interface (Section III-A), the negative-sequence controller with current limiting, and the voltage/current cascade.

A. Electromechanical Subsystem

The VSM emulates the inertia and damping of a synchronous machine through the per-unit swing equation [9]–[11],

$$\frac{d\omega_{pu}}{dt} = \frac{1}{T_H}\left(P_{\mathrm{ref}} - P_{\mathrm{meas},f} - P_{\mathrm{damp}}\right), \tag{1}$$

$$\frac{d\theta}{dt} = 2\pi f_0\, \omega_{pu}, \tag{2}$$

where $T_H = 1$ s is the virtual inertia time constant, $f_0 = 50$ Hz, and $P_{\mathrm{meas},f}$ is the active power filtered with a 1 ms time constant. P_{damp} is a damping power saturated to $[-0.6, +0.7]$ pu, made of a term proportional to the speed deviation (damping coefficient 1.056) and a 10% primary-frequency droop on the measured grid frequency, itself filtered with a 0.15 s time constant. The default tuning is unstable at SCR ≥ 5 regardless of the extraction method (Section V-A); doubling the damping coefficient to 2.112 with default limits gives a clean baseline for SCR $\in \{1.5, 3, 5\}$ and is used throughout. The virtual angle θ is also the angle of every Park transform in the controller and the extractors, so extraction error can reach the VSM through the injection loop.

B. Inner Control Loops and Current Limiting

The inner loops form a single positive-sequence dq cascade referenced to θ: an outer PI voltage controller produces current references, which are clamped by dynamic limits and regulated by an inner PI current controller with decoupling and anti-windup. There is no separate negative-sequence current loop. Current limiting uses the virtual-impedance variant of Paquette and Divan [12]: once the converter is in overcurrent, a voltage perturbation computed from the positive-sequence current is subtracted from the nominal voltage references,

$$V_{md,\mathrm{final}} = V_{md}^{*} - \Delta V_d, \qquad V_{mq,\mathrm{final}} = V_{mq}^{*} - \Delta V_q. \tag{3}$$

C. Negative-Sequence Injection

Negative-sequence regulation is a structural extension of this mechanism and not an independent loop, consistent with [2]. It is the point at which the extractor output enters the control architecture. From the negative-sequence voltage $V_{\mathrm{neg},dq}$ of the extraction interface, a current reference is generated as a feed-forward rotation,

$$I_{\mathrm{neg},dq} = g \cdot k_{\mathrm{neg}} \cdot R(\varphi_c) \cdot V_{\mathrm{neg},dq}, \tag{4}$$

where $g \in [0, 1]$ is a smooth deadband gate that is zero below 0.05 pu and one above 0.10 pu on $|V_{\mathrm{neg},dq}|$ (5 ms low-pass filter), $k_{\mathrm{neg}} = 2$ for DSOGI-FLL, DSC and the EKF and $k_{\mathrm{neg}} = 0.25$ for ST-SMO (whose injection loop is not stable at higher gain, Section V-D), and $R(\varphi_c)$ is a rotation of the dq-complex vector by $\varphi_c = -13°$. A continuous ramp is used because a hard relay produced a self-sustained oscillation during development. The reference is saturated to the standard's current-sharing limit ($0.5\, I_{\max}$) and converted to a voltage perturbation through a virtual impedance $R_{\mathrm{neg}} + jX_{\mathrm{neg}} = 0.1 + j1.0$ pu,

$$\Delta V_{d,\mathrm{neg}} = R_{\mathrm{neg}} I_{\mathrm{neg},d} - X_{\mathrm{neg}} I_{\mathrm{neg},q}, \tag{5}$$

$$\Delta V_{q,\mathrm{neg}} = X_{\mathrm{neg}} I_{\mathrm{neg},d} + R_{\mathrm{neg}} I_{\mathrm{neg},q}, \tag{6}$$

which is limited to ± 1 pu, rate-limited, and added to the same $V_{md,\mathrm{final}}/V_{mq,\mathrm{final}}$ references as the positive-sequence perturbation. All injection parameters are listed in Table I.

The commanded angle φ_c is not the lead of the realized current. Two effects separate them. In the positive-sequence dq frame a negative-sequence component rotates clockwise, so a counter-clockwise rotation by $+\varphi$ is a phase *lag* of φ for the time signal; and the virtual impedance (argument $84.3°$) and the voltage loop rotate the realized current again. To first order, a realized lead of $95°$ needs a commanded angle $\varphi^{*} \approx -95° + 84.3° = -10.7°$ (here $*$ marks the first-order required value of φ_c), and a calibration (DSC, three SCR, SLG, LL, LLG) gave $-10.4°$ to $-18.7°$ in eight of nine cases (the ninth, SCR 1.5 LLG, has a voltage collapse). The commanded angle is therefore a tuned parameter of this plant, and $\varphi_c = -13°$ places the realized lead of DSOGI-FLL and the EKF inside the band, in its upper half (Section IV-B). With $\varphi_c = +95°$ the realized lead was in the band in none of 36 cases.

The rate limiter must be sized to the 100 Hz carrier. In the extractors' dq frame the perturbation is a $2\omega = 100$ Hz signal, so a limit S passes an amplitude of at most $S/(2\pi \cdot 100)$. The required perturbation (about 0.36 pu for DSC at SCR 3, SLG) needs about 226 pu/s, whereas the originally configured 40 pu/s passes 0.064 pu and left the injection almost without authority; a limit of 500 pu/s is therefore used for all methods. Everything computed with the original limit was obtained with the injection effectively disabled.

Only the lead-angle requirement is used as a compliance criterion, and it is assessed on the realized current (Section IV); the realized magnitude is reported descriptively.

III. Extraction Interface and Methods

All four methods sit behind one interface that takes the three-phase point-of-coupling voltage V_{abc} and the virtual angle θ and returns $V_{\mathrm{pos},dq}$, $V_{\mathrm{neg},dq}$ and an estimated angular frequency $\hat{\omega}$. All four share the same Clarke and Park stages and differ only in the block that computes $V_{\mathrm{pos},\alpha\beta}$ and $V_{\mathrm{neg},\alpha\beta}$ from $V_{\alpha\beta}$. Table I lists their parameters, and Fig. 2 shows the four signal paths.

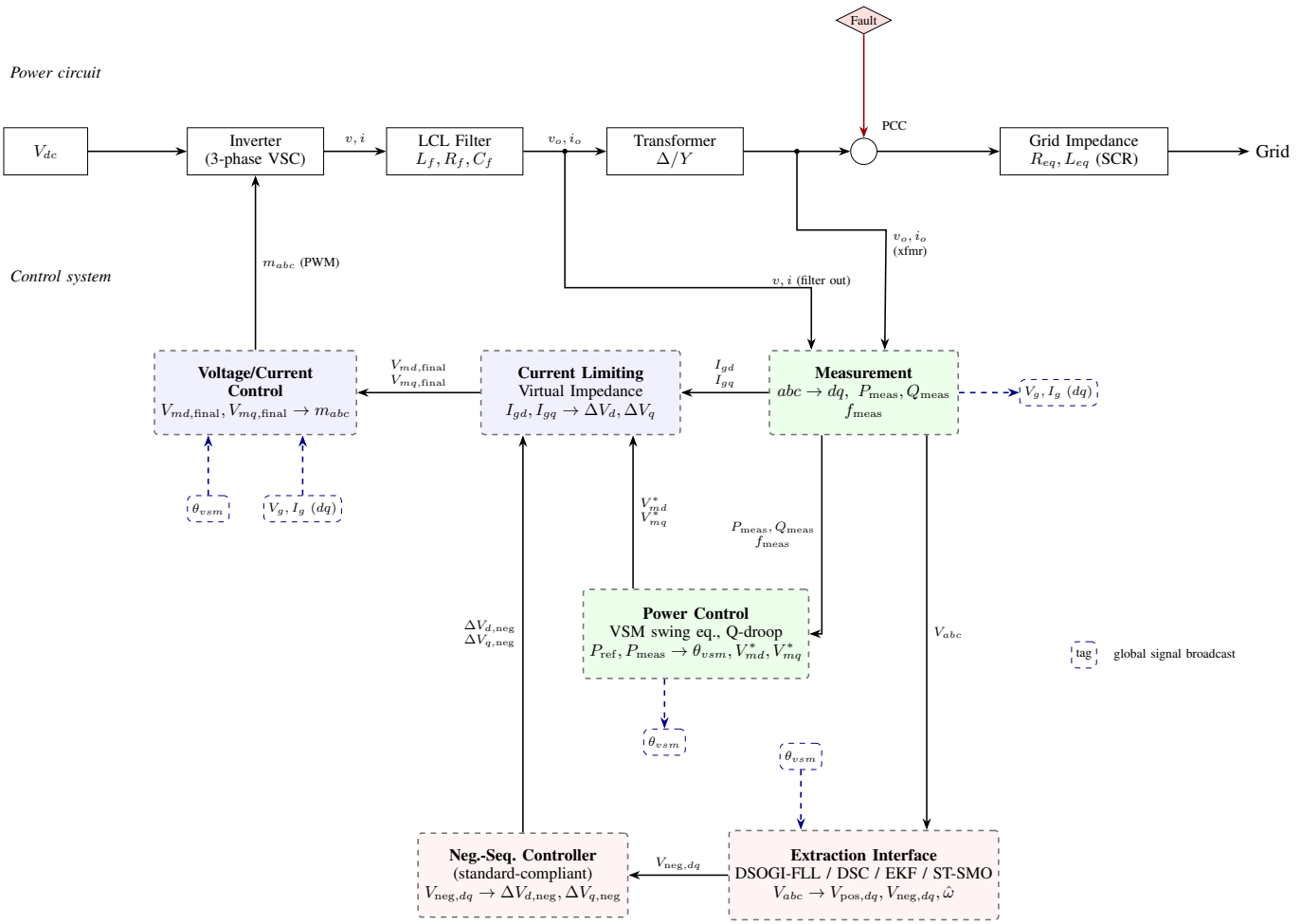


Fig. 1. Overall subsystem interconnection: the power circuit (top) and the control architecture (bottom), showing the extraction interface (Section III) and negative-sequence controller (Section II-C) in the context of the full control loop. A superscript $*$ denotes a reference value.

TABLE I
SYSTEM, EXTRACTOR, INJECTION AND TEST PARAMETERS USED THROUGHOUT

VSM and plant	
Nominal frequency	$f_0 = 50$ Hz
Virtual inertia time constant	$T_H = 1$ s
Damping coefficient	1.056 (default); 2.112 (used)
Damping-power limits	$[-0.6, +0.7]$ pu
Frequency droop	10%
Power-measurement filter	1 ms
Frequency-measurement filter	0.15 s
Grid	series RL, $X/R = 5$, SCR $\in \{1.5, 3, 5\}$ (SCR 10 excluded)
Controller sample time	$T_s = 50$ μs (extractor harness: 100 μs)
Test protocol	
Faults	SLG, LL, LLG, 3ph
Profiles	permanent; cleared after 0.10 s; cleared after 0.35 s
Disturbance instant	$t = 3$ s
Realized-current fit window	last 0.2 s
Ground-truth fit window	last 100 ms
Ripple (tail) window	last 20 ms

Extractors	
DSOGI-FLL	$k = \sqrt{2}$, $\Gamma = 50$, $\hat{\omega}$ limited to $\pm 20\%$
DSC	delay $N_d = T_0/4T_s = 100$ samples at 50 μs
EKF	$Q = \text{diag}(10^{-6}, 10^{-6}, 10^{-6}, 10^{-6}, 10^{-4})$, $R = 10^{-4} I_2$, $P_0 = 0.1 I_5$, $x_0 = [1, 0, 0, 0, 2\pi \times 50]^\top$
ST-SMO	$\lambda_1 = 600$, $\lambda_2 = 150{,}000$, $\omega_0 = 2\pi \times 50$
Negative-sequence injection	
Virtual impedance	$R_{\text{neg}} + jX_{\text{neg}} = 0.1 + j1.0$ pu
Gate thresholds	0.05 / 0.10 pu on $\lvert V_{\text{neg}} \rvert$ (5 ms low-pass)
Gain k_{neg}	2 (DSOGI-FLL, DSC, EKF); 0.25 (ST-SMO)
Commanded angle φ_c	-13°
Current-reference limit	$0.5\, I_{\max}$
ΔV limit; rate limit	± 1 pu; 500 pu/s

A. Symmetrical Components and the Common Structure

Fortescue showed that any unbalanced three-phase set is the sum of positive-, negative- and zero-sequence sets [13]. A real-time controller needs this separation sample by sample, so the three phase signals are first mapped to a two-axis stationary frame by the Clarke transform [14], in which a positive-sequence component traces a counter-clockwise circle and a negative-sequence component a clockwise one. Separating them requires, for each of V_α and V_β, a *quadrature companion*: a copy lagging by 90° at the instantaneous frequency. Adding or subtracting these companions gives the positive- and negative-sequence components in the stationary frame (the PNSC algebra of Fig. 2). The Park transform [15], referenced to the virtual angle θ, then makes the positive sequence a DC quantity and the negative sequence a $2\omega = 100$ Hz oscillation. The inner PI loops cannot regulate such an oscillation, which is why negative-sequence current is regulated by the separate injection of Section II-C and not by a second loop in the same frame. The four methods are four ways of generating the quadrature companion when the true frequency is unknown and may itself be disturbed by the fault [16]. $\hat{\omega}$ is logged but not used by the controller, so frequency adaptation acts only through estimation accuracy away from nominal frequency.

B. DSOGI-FLL

A second-order generalized integrator (SOGI) on each of V_α and V_β produces an in-phase estimate x_1 and a quadrature estimate x_2 at a shared center frequency $\hat{\omega}$, which a frequency-locked loop (FLL) adapts [17]:

$$\dot{x}_1 = \hat{\omega}\,[k(v - x_1) - x_2]\,, \qquad \dot{x}_2 = \hat{\omega}\,x_1, \tag{7}$$

$$\dot{\hat{\omega}} = -\Gamma\,[(v_\alpha - x_{1,\alpha})\,x_{2,\alpha} + (v_\beta - x_{1,\beta})\,x_{2,\beta}]\,, \tag{8}$$

with $\hat{\omega}$ saturated to $\pm 20\%$ of nominal and delayed by one sample to avoid an algebraic loop. The sequence components are

$$V_{\mathrm{pos},\alpha} = \tfrac{1}{2}(x_{1,\alpha} - x_{2,\beta}), \quad V_{\mathrm{pos},\beta} = \tfrac{1}{2}(x_{2,\alpha} + x_{1,\beta}), \tag{9}$$

$$V_{\mathrm{neg},\alpha} = \tfrac{1}{2}(x_{1,\alpha} + x_{2,\beta}), \quad V_{\mathrm{neg},\beta} = \tfrac{1}{2}(x_{1,\beta} - x_{2,\alpha}). \tag{10}$$

The gains are $k = \sqrt{2}$ and $\Gamma = 50$. The two integrators use trapezoidal discretization, because forward Euler introduces a gain bias of order $\hat{\omega}T_s/k$. Under balanced steady state $V_{\mathrm{pos},dq}$ matches the plant to within 0.01% and $\hat{\omega}$ settles to $2\pi \times 50$ rad/s.

C. Delayed Signal Cancellation (DSC)

A delay of a quarter of the nominal period is a 90° shift at nominal frequency, so combining a signal with its delayed copy cancels one sequence [18]. With $V_{\alpha,d}, V_{\beta,d}$ delayed by $T_0/4$ (100 samples at $T_s = 50$ μs),

$$V_{\mathrm{pos},\alpha} = \tfrac{1}{2}(V_\alpha - V_{\beta,d}), \quad V_{\mathrm{pos},\beta} = \tfrac{1}{2}(V_\beta + V_{\alpha,d}), \tag{11}$$

$$V_{\mathrm{neg},\alpha} = \tfrac{1}{2}(V_\alpha + V_{\beta,d}), \quad V_{\mathrm{neg},\beta} = \tfrac{1}{2}(V_\beta - V_{\alpha,d}). \tag{12}$$

There is no adaptive element, and $\hat{\omega}$ reports the nominal value. Under balanced steady state DSC reproduces the plant exactly ($V_{\mathrm{pos},dq} = [0.9976, 0.0000]$ pu).

D. Extended Kalman Filter (EKF)

The EKF holds the positive- and negative-sequence $\alpha\beta$ components and the frequency in the state $x = [V_{\mathrm{pos},\alpha}, V_{\mathrm{pos},\beta}, V_{\mathrm{neg},\alpha}, V_{\mathrm{neg},\beta}, \omega]^\top$, an $\alpha\beta$-frame formulation with the frequency as a state, as in [19]. A stationary complex-valued Kalman filter for the same task is given in [20]. With $\vartheta = T_s x_5$, the process model rotates the positive pair by $+\vartheta$ and the negative pair by $-\vartheta$ exactly,

$$x_{pred} = \begin{bmatrix} \cos\vartheta\, x_1 - \sin\vartheta\, x_2 \\ \sin\vartheta\, x_1 + \cos\vartheta\, x_2 \\ \cos\vartheta\, x_3 + \sin\vartheta\, x_4 \\ -\sin\vartheta\, x_3 + \cos\vartheta\, x_4 \\ x_5 \end{bmatrix}, \tag{13}$$

the covariance is propagated as $P_{pred} = FPF^\top + Q$ with $F = \partial x_{pred}/\partial x$, and the measurement $z = [V_\alpha; V_\beta]$ with $H = \begin{bmatrix} 1 & 0 & 1 & 0 & 0 \\ 0 & 1 & 0 & 1 & 0 \end{bmatrix}$ gives the standard correction $K = P_{pred}H^\top(HP_{pred}H^\top + R)^{-1}$, $x = x_{pred} + K(z - Hx_{pred})$. $\hat{\omega} = x_5$. The covariances and initial state are in Table I. The exact rotation is used because its small-angle approximation has determinant $1 + \vartheta^2$ and biases the estimate high by about 1.1%.

E. Super-Twisting Sliding-Mode Observer (ST-SMO)

The super-twisting differentiator of Levant [21] is applied to V_α and V_β separately. With sliding variable $s = x_1 - v$,

$$x_{1,new} = x_1 + T_s\left(-\lambda_1\sqrt{|s|}\,\mathrm{sign}(s) + x_2\right), \tag{14}$$

$$x_{2,new} = x_2 + T_s\,(-\lambda_2\,\mathrm{sign}(s))\,, \qquad \hat{q}v = -x_{2,new}/\omega_0, \tag{15}$$

where x_1 tracks v and x_2 tracks $\dot{v}$; for $v = A\cos\omega t$ the rescaled $-\dot{v}/\omega$ is the quadrature companion. The sequence components then follow from the same algebra as DSOGI-FLL, with $(x_1, \hat{q}v)$ as the in-phase/quadrature pair. Convergence requires λ_2 to exceed the Lipschitz bound $L = A\omega^2 \approx 98{,}700$; with 1.5 times margin and $\lambda_1 \approx 1.5\sqrt{\lambda_2}$ this gives $\lambda_1 = 600$ and $\lambda_2 = 150{,}000$. Under balanced steady state the method converges to $V_{\mathrm{pos},dq} = [0.9909, 0.0021]$ pu (0.67% low) with a negative-sequence leakage of about 3% ($V_{\mathrm{neg},dq} \approx [0.007, 0.030]$ pu). This residual is treated as a characteristic of discrete super-twisting differentiation and its consequences are reported, not corrected.

IV. Model Validation

No hardware is used, so every check is made against a reference independent of the code under test: closed-form theory, the standard itself, an identity of circuit physics, or a refined numerical solution. Following Roache [22], *verification* asks whether the equations are solved correctly and *validation* whether they agree with an independent reference. Four checks address four failure classes: extractor implementation, realized-versus-commanded current, plant and measurement consistency, and numerical convergence.

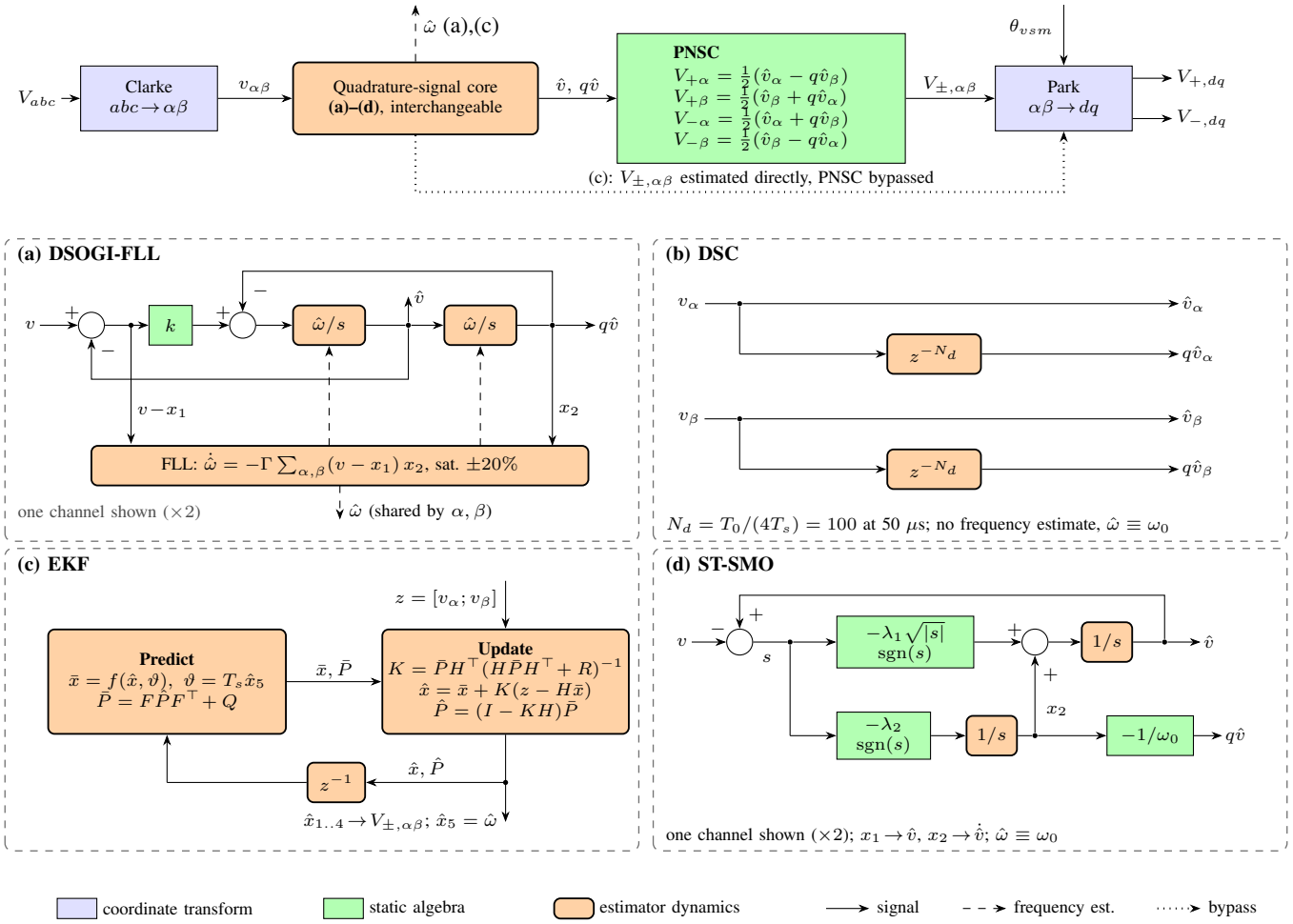


Fig. 2. Common extraction interface and the four interchangeable quadrature-signal cores. The Clarke and Park transforms and the positive/negative-sequence calculation (PNSC) are shared; each core produces an in-phase estimate $\hat{v}$ and its quadrature companion $q\hat{v}$ for α and β, except the EKF, which estimates the sequence components directly. (a) DSOGI-FLL, one channel of two with a shared frequency-locked loop; (b) DSC; (c) EKF; (d) ST-SMO, one channel of two. Blue: coordinate transform; green: static algebra; orange: estimator dynamics. Dashed: frequency estimate; dotted: PNSC bypass.

A. Extractors Against an Analytic Truth

Each extractor is run in a standalone harness, built from the unmodified variant subsystems, on synthetic three-phase voltages whose sequence components are known analytically: two unbalanced sags of 0.5 pu with the negative sequence in phase or in antiphase with the positive sequence [23], a 30° positive-sequence phase jump, a step in frequency from 50 to 49 Hz, and a balanced fundamental with 5th (5%, negative sequence) and 7th (3%, positive sequence) harmonics, for which the fundamental components are the truth. The frequency step is the one disturbance on which the methods differ structurally.

The pass criteria were fixed in advance. The steady-state combined error in V_{pos} and V_{neg}, taken as the mean magnitude over the last 0.1 s, must be at most 0.010 pu for DSOGI-FLL, DSC and the EKF on the three nominal-frequency disturbances, and the DSC offset on the frequency step must equal the analytic value for a fixed quarter-period delay seen at 49 Hz. Settling is the time to enter and remain within 0.02 pu on a 2.1 ms median-filtered error, where 0 ms means that the error never left the band. The harmonic case has no threshold.

Outcome (Fig. 3). On the nominal-frequency disturbances DSC reproduces the sequence components to numerical precision ($\leq 3\times10^{-14}$ pu), as expected of an algebraic method at its design frequency; DSOGI-FLL reaches 3×10^{-5}–4×10^{-4} pu and the EKF 2×10^{-5}–2×10^{-4} pu. ST-SMO settles at 0.036–0.039 pu and exceeds the criterion, which is reported as a property of the method. Settling takes 4.9–5.0 ms for DSC, 9.2–13 ms for the EKF and 11.9–15 ms for DSOGI-FLL, and ST-SMO never settles. On the frequency step the EKF follows the truth to 2×10^{-4} pu, and DSC shows a constant offset of 0.0222 pu, equal to within 0.1% to the analytic value $\sqrt{2}\,\epsilon/2$ with $\epsilon = (\pi/2)(1 - 49/50) = 0.0314$ rad. DSOGI-FLL ends at 0.0285 pu with the error still falling at the end of the 0.5 s window; in an 11 s repeat it enters the band after 1994 ms and its error in the last second is 0.0036 pu, so its frequency loop converges, but slowly. ST-SMO ends at 0.042 pu.

On the harmonic case the errors are 0.0107 pu for DSOGI-FLL, 0.0371 pu for the EKF, 0.0546 pu for DSC and 0.206 pu for ST-SMO. DSC is exact in V_{pos}, but its V_{neg} error of 0.0546 pu (peak 0.08 pu, the sum of the two harmonic amplitudes) shows that both harmonics, one of positive and one of negative sequence, appear in V_{neg}; this is consistent

with a quarter-period delay rotating a component of order h by $h \cdot 90°$, but was not tested separately. Clean-signal accuracy therefore does not predict closed-loop noise (Section V-B).

B. Realized Negative-Sequence Current Against the Standard

Method. IEEE 2800-2022 constrains the *realized* negative-sequence current, so this check uses no extractor output and no controller signal. For permanent SLG, LL and LLG faults at SCR $\in \{1.5, 3, 5\}$ and all four methods (36 runs), the raw plant voltages V_{gd}, V_{gq}, currents I_{gd}, I_{gq} and the unwrapped VSM angle over the last 0.2 s are expressed as complex dq vectors and fitted by complex least squares to $z = A + B\,e^{-j2(\theta-\theta_0)}$, where θ_0 is a constant reference angle. Here $|A|$ and $|B|$ are the positive- and negative-sequence magnitudes, B_i/B_v is the realized current-to-voltage relation, and the lead in phasor convention is $\varphi_{\text{lead}} = -\arg(B_i/B_v)$. The sign of the current is taken from the direction of the pre-fault active power (the pre-fault power ratio is 1.00 in all 36 final-design cases, so the current is positive out of the converter). The pass criterion, and the only compliance criterion used, is a realized lead of 90°–100°. A case is a valid measurement if the pre-fault sign and scale check holds (power ratio 0.95–1.05) and the fit residuals of voltage and current are at most 0.10 pu.

Outcome 1: the commanded angle does not establish compliance (Fig. 4). With the controller as first configured ($\varphi_c = +95°$, 40 pu/s limit) the reference leads V_{neg} by exactly $+95.00°$, yet the realized lead was $-142°$ to $-176°$ (median $-158°$) in 32 of the 36 cases and in none of the 36 within the band. The two causes are derived in Section II-C.

Outcome 2: final design ($k_{\text{neg}} = 2$, $\varphi_c = -13°$, 500 pu/s for DSOGI-FLL, DSC and the EKF; $k_{\text{neg}} = 0.25$ for ST-SMO). The leads below come from the $\alpha\beta$-frame fit at $T_s = 50$ μs (Section IV-D); the θ-based fit at 100 μs gives the same in-band counts, with leads that differ by at most 0.3° (DSOGI-FLL), 0.6° (EKF), 1.5° (DSC) and 2.4° (ST-SMO). All 36 measurements are valid (fit residuals at 100 μs at most 0.09 pu for the smooth methods and 0.04 pu for ST-SMO). The realized lead lies inside the band in 24 of the 27 smooth-extractor cases (DSOGI-FLL 8/9, DSC 8/9, EKF 8/9); the three exceptions are all SCR = 1.5 LLG, with leads of 128°–131° under voltage collapse. In the other cases DSOGI-FLL realizes 95.7°–99.6° and the EKF 95.6°–99.9°, whereas DSC realizes a lead 1.7°–3.3° lower than DSOGI-FLL (92.5°–97.7°), the lowest being 92.5° at SCR 1.5 SLG. At $k_{\text{neg}} = 0.25$ the ST-SMO injection is stable but nearly inactive: its realized lead is 144°–146° in 8 of 9 cases ($-179°$ at SCR 1.5 LLG), none is in band, and its realized $|I_{\text{neg}}|/|V_{\text{neg}}|$ is about 0.35 against about 1.15 for the others. A higher-gain design ($k_{\text{neg}} = 6$) was worse (7 of 36 in band, with a spread of about 10° across the smooth methods), which is why the lower gain is adopted.

Cross-check and caveat. Refitting the realized currents of the same 36 runs at 100 μs in the $\alpha\beta$ frame, without θ, gives 24 of 36 leads in band as before, with differences of at most 0.02°, so the logged angle is not a source of error. Both fits use the same fundamental model; the residual is third-harmonic and kHz content generated by the injection, which the power identity accounts for (Section IV-C). The SCR 1.5 LLG cases, with the highest residuals (0.07–0.08 pu), are the least certain.

Temporary faults. DSOGI-FLL, DSC and the EKF were stable in all 36 temporary-fault runs (SCR 1.5 and 3, 0.10 and 0.35 s clearing), with a post-clearing $|V_{\text{neg}}|$ tail of at most 6×10^{-5} pu and a peak $|I_g|$ of 0.98–1.09 $I_{\max}$; ST-SMO at $k_{\text{neg}} = 2$ keeps oscillating in all 12 runs (Section V-D).

C. Plant and Measurement Self-Consistency

Park/angle chain. The dq voltage computed from the raw phase voltages and the logged virtual angle coincides with the plant's own V_{gd}, V_{gq} to 1.6×10^{-11} % to 2.0×10^{-11} % (relative RMS) in all 48 permanent-fault runs, so the logged angle is the one used by the plant's Park transform.

Instantaneous-power identity. Under unbalance the 2ω component of the instantaneous power is fully determined by the sequence phasors [24]. The logged active power carries no 100 Hz content, so the reference is the instantaneous power of the raw phase quantities, $p_{abc} = v_a i_a + v_b i_b + v_c i_c$, over the last 0.2 s. The prediction uses the fitted dq vectors of Section IV-B: with the amplitude-invariant Clarke transform, $p(t) = P_{\text{dc}} + \text{Re}\{C\,e^{-j2\psi(t)}\}$, $\psi(t) = \theta(t) - \theta_0$, $C = \frac{3}{2}(\bar{A}_v B_i + B_v \bar{A}_i)$, with P_{dc} the mean power, and the measured 100 Hz component comes from regressing p_{abc} on $\{1, \cos 2\psi, \sin 2\psi\}$. The criterion is an amplitude ratio within $\pm 10\%$ and a phase error within 5°. The test checks the model's own signals and is not an independent plant validation.

Outcome. With the two-sequence model the identity fails for the smooth extractors in the 36 final-design runs at 50 μs: the amplitude ratio is within $\pm 10\%$ in 12 and the phase error within 5° in 9, and only 8 runs satisfy both (median ratio 1.168, median |phase| 15.0°, maximum 30.2°), almost all of them ST-SMO, whose injection is nearly inactive; the 100 μs runs give the same counts. The ratio of p_{abc} to the pre-fault P_{meas} is 1.50 in every run, the factor $3/2$ between the amplitude-invariant raw power and the per-unit P_{meas}, so the scale check holds. A spectrum of the residual of the $\alpha\beta$ fit (DSC, SCR 3, SLG, 100 μs) identifies the missing content. It is absent with the injection off (residual 0.0000) and small at $k_{\text{neg}} = 0.25$ (0.004 of the voltage norm, 0.008 of the current norm); at $k_{\text{neg}} = 2$ (0.034 and 0.048) it is concentrated at ± 150 Hz, that is third-harmonic content (voltage 0.024 and 0.008 pu, current 0.044 and 0.003 pu), with further lines near 3 kHz, and the 150 Hz lines grow by a factor of 6.4 for an eightfold gain. These components beat with the fundamental positive sequence to give 100 Hz power. When tones at $\pm 3\omega$ are added to the fit, the identity holds in all 36 runs at both steps for all four methods (amplitude ratio 0.999–1.006, |phase| $\leq 0.6°$). The fundamental phasors of the fit, from which the leads of Section IV-B are taken, are therefore consistent with the raw power once the injection-generated third-harmonic content is included, and the failure of the two-sequence model was an omitted-tone effect and not an error in the leads. The origin of the 150 Hz and kHz content was not identified.

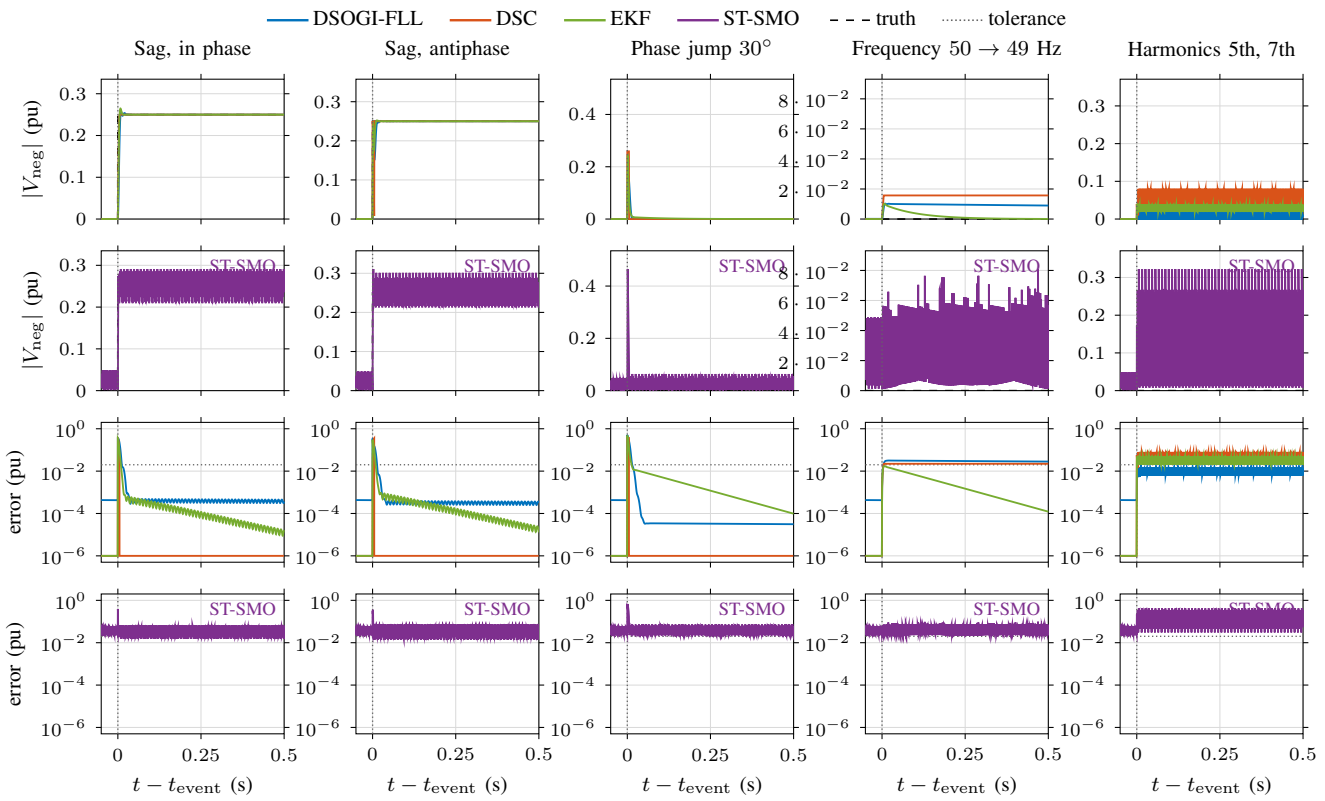
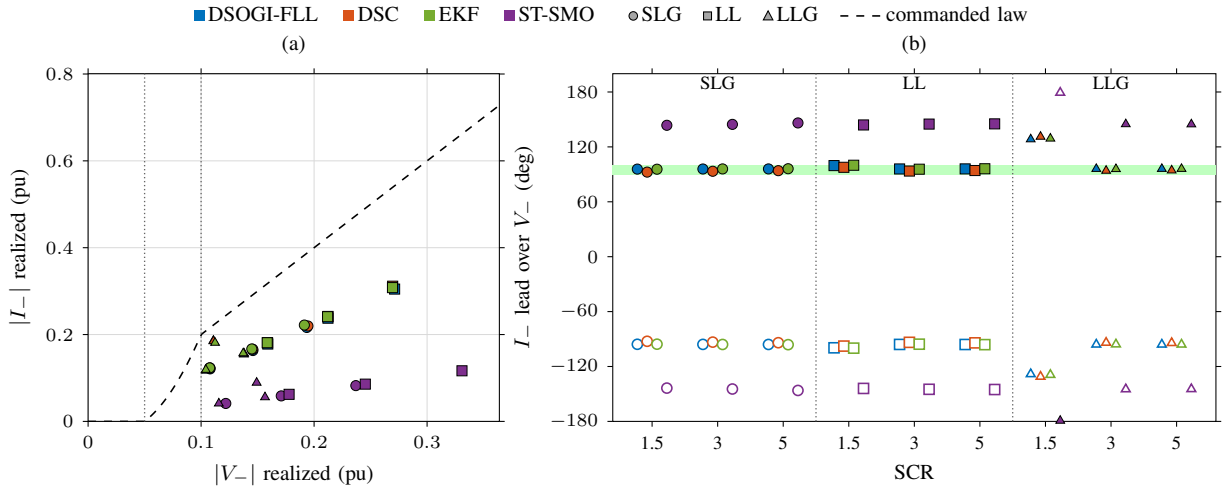


Fig. 3. Extractor behavior against the analytic truth for the five synthetic cases (sag in phase, sag in antiphase, phase jump, frequency step, harmonics), one row per method and one column per case; the error floor is 10^{-6} pu and the steady-state tolerance is dotted.



filled: phasor convention (IEEE 2800); hollow: raw dq-complex angle; shaded band: 90°–100°

Fig. 4. Realized negative-sequence behavior from raw plant signals. (a) $|I_{neg}|$ against $|V_{neg}|$ with the gated control law (drawn for $k_{neg} = 2$) and the deadband thresholds. (b) Realized lead angle in phasor convention against the 90°–100° band of IEEE 2800-2022; colour marks the method and the marker the fault type. Fit at $T_s = 50$ μs.

D. Numerical Convergence

The SCR 3 permanent SLG, LL and LLG cases are run at $T_s = 100$, 50 and 25 μs, rescaling every sample-time field of the controller, the DSC delay and the model step. The criterion, fixed when the results were examined and not before, is that between 50 and 25 μs the peak $|V_{neg}|$ changes by less than 5 % and the RMS differences in $|V_{neg}|$ and P_{meas} are below 0.01 pu, evaluated from 0.02 s before to 0.30 s after the disturbance. DSOGI-FLL and DSC meet it for all three faults. The EKF meets the RMS limits but not the peak limit (−9.5 to −12.7 %); its covariances are defined per sample and were not rescaled, so the effect of the step and that of the implied noise intensity were not separated, and its median $|V_{neg}|$ ripple in the sweep is 0.0086 pu at 100 μs and 0.0101 pu at 50 μs. ST-SMO ($k_{neg} = 0.25$) meets the peak and power limits but not the RMS limit on $|V_{neg}|$ (0.028–0.038 pu, comparable to

its ripple), so the waveform of its chatter is not reproduced from one step to the next, and the fourfold fall of its error predicted by a discretization ripple $T_s\lambda_2/\omega_0$ is not observed (post-clearing tail 0.024, 0.035 and 0.025 pu at 100, 50 and 25 μs).

The plant response is a different matter, and 100 μs is not converged for LL and LLG. At SCR 3 the power response at 100 μs departs from that at 25 μs from 45 ms after the fault and differs by an RMS of 0.30–0.56 pu for all four methods, whereas 50 μs agrees with 25 μs to within 0.0037 pu; for SLG the 100 μs difference is at most 0.011 pu. For temporary faults (DSC) the recovery time falls from 100 to 50 μs by 1.20 and 0.32 s for LL and by 0.97 and 0.51 s for LLG (0.10 and 0.35 s clearing) and the peak rotor-angle deviation by 8°–24°, whereas from 50 to 25 μs it changes by at most 0.001 s and 0.03°. A step of 50 μs is therefore used for the sweep, the ground-truth reconstruction and the lead and power-identity checks. Between the two sweeps 17 of the 96 recovery times differ by more than 0.1 s, 15 of them for LL and LLG at SCR 3, and the rotor angle changes by more than 2° only there. The ground-truth reconstruction is also run at 50 μs (Section V).

No hardware or cross-platform replication is available and no small-signal analysis is attempted, which is the territory of Awal *et al.* [7]. The claims of this paper concern *relative* method performance inside one fixed architecture.

V. Results

All results use the full-order VSM of Section II with the final injection design (Section II-C), for the four extraction methods at SCR $\in \{1.5, 3, 5\}$, $X/R = 5$ and four fault types (SLG, LL, LLG, three-phase). Each of the 48 method–SCR–fault combinations is run with a permanent fault and with temporary faults cleared after 0.10 s (primary protection, five cycles) and 0.35 s (breaker-failure backup), giving 144 simulations. Disturbances are applied at $t = 3$ s, runs end at $t = 8$ s and $T_s = 50$ μs (Section IV-D). The pre-fault active power is about 0.75 pu in every run (0.753, 0.750 and 0.750 pu at SCR 1.5, 3 and 5). ST-SMO is run at $k_{\text{neg}} = 0.25$, where its injection is nearly inactive (Section IV-B), so its regulation and recovery results are not comparable in kind with those of the other three and are reported as such. SCR $= 10$ was also simulated (a further 48 simulations) and is characterized separately in Section V-A.

Metrics. Settling time is the time after the disturbance for $|V_{\text{neg},dq}|$ to enter and remain within a band about its settled value (the mean over the last 20 ms), the band being the largest of 5 % of that value, three standard deviations of the last 20 ms and 0.005 pu; a single sample outside the band restarts the clock, so the criterion is fragile. *Steady-state ripple* is the standard deviation of $|V_{\text{pos},dq}|$ and $|V_{\text{neg},dq}|$ over the last 20 ms. *Rotor-angle deviation* is the peak deviation of the unwrapped virtual angle from a linear trend fitted to its pre-fault behavior. *Complexity* is the static block count of each method's variant subsystem. *Recovery* follows Clause 7.2.2.6 of the standard: active power is to be restored within 1.0 s of the voltage returning to the continuous-operation region, with a tolerance on that *time* of the greater of ± 0.2 s or $\pm 10\%$, so recovery up to 1.2 s is taken as compliant. The recovery time is measured from fault clearing to the instant after which P_{meas} stays within $\max(10\%\,|P_{pre}|, 0.01\text{ pu})$ of its pre-fault level; a run that does not remain within the band to the end is counted as not recovered. The 10% band on the power is a choice of this study and not a requirement of the standard.

Extraction-induced regulation error. Once the gate is open and the current is not saturating, the controller's current reference is an algebraic function of the estimated $V_{\text{neg},dq}$, so its deviation from the controller's own law is at numerical precision in all 36 unbalanced runs (at most 6.4×10^{-15} %) and cannot discriminate between methods; it is retained only as a consistency check. The discriminating quantity is the error of the regulated current, in size and angle together, relative to the current the same law would command from the *true* negative-sequence voltage, reconstructed offline from the raw phase voltages and independent of the four estimators.

Ground-truth reconstruction. Over a settled window of 100 ms the stationary-frame voltage $w(t) = V_\alpha + jV_\beta$ is the sum of a positive- and a negative-sequence rotating vector, $w(t) = P\,e^{j\omega t} + N\,e^{-j\omega t}$. A complex least-squares fit, with ω found by a one-dimensional search, recovers P, N and ω; $|N|$ is the true negative-sequence magnitude, and the true vector in the VSM's dq frame is $N\,e^{-j(\omega t+\theta(t))}$, so every estimator is compared with a reference that uses the same angle. The reference is computed offline over the whole window, which no causal estimator can do. For three-phase faults the true negative sequence is zero and the absolute leakage is reported. The fit residual is 1.2–7.7 % of $\|w\|$ for DSOGI-FLL, DSC and the EKF and 0.4–3.5 % for ST-SMO (11–46 % and 3.7–16 % of the negative-sequence term); as for the realized-current fit it is non-fundamental content generated by the injection (Section IV-C). Two checks support the reference: $|N|$ agrees with the independent DSOGI-FLL estimate to within 0.27 %, and refitting N on two non-overlapping 40 ms windows agrees to within 0.42 % and 0.24° in all 36 unbalanced runs. The ground-truth runs use $T_s = 50$ μs, like the sweep.

A. VSM Stability and SCR-Dependent Tuning

The base VSM ($T_H = 1$ s, damping coefficient 1.056, default limits) is unstable at SCR $= 5$ and 10 independent of the extraction method and the injection. For SCR $\in \{1.5, 3, 5\}$ doubling the damping coefficient (2.112, default limits) is clean: 12 of 12 cases on DSOGI-FLL over the full fault grid and every screened case on the other methods, and the 144-simulation sweep completed without a simulation error. This tuning is used for all comparative results.

At SCR $= 10$ no validated retuning exists. The candidate examined (damping $\times 4$, limits widened to ± 2 pu) passes a screen based on the virtual speed, but the measured active power shows, with no fault applied, a sustained oscillation of about 4 Hz with a peak-to-peak amplitude of 1.4–1.8 pu, identical across the four methods. It is therefore a limit cycle of the base VSM and grid model and not of the extraction, and the fault results obtained under this candidate are discarded. A plausible mechanism, not verified, is the 0.15 s low-pass filter of the measured frequency, which contributes about 75°

of lag at 4 Hz. That the default tuning fails at high and not at low SCR is the opposite of the usual weak-grid expectation [8] and suggests that the VSM's own damping structure sets the limit.

B. Settling Time, Ripple, Regulation Accuracy and Rotor-Angle Deviation

Settling time. In the sweep (permanent faults, three-phase faults excluded because their true negative-sequence voltage is zero) the medians over the nine unbalanced cases are 258 ms for DSOGI-FLL, 23 ms for DSC, 24 ms for the EKF and 1801 ms for ST-SMO (Table II). The spread within each method (for example DSOGI-FLL 46–1541 ms) is larger than the difference between DSC and the EKF, and the values are not monotonic in SCR (DSOGI-FLL, LL: 689, 46 and 258 ms), so only a coarse statement is made: ST-SMO is the slowest and most variable, with three values at the end of the 5 s post-disturbance window that are not interpreted.

Ripple. In the closed loop, excluding three-phase faults, the ripple of $|V_{\mathrm{neg},dq}|$ has medians of 0.0032, 0.0161, 0.0101 and 0.0429 pu for DSOGI-FLL, DSC, the EKF and ST-SMO (Table II). DSC applies no filtering and passes the harmonic content of the plant directly (Section IV-A), so its $|V_{\mathrm{neg}}|$ ripple is five times that of DSOGI-FLL although it is exact on clean signals. The ripple of ST-SMO is 2.7, 4.2 and 13 times that of DSC, the EKF and DSOGI-FLL, and at $k_{\mathrm{neg}} = 0.25$ it is largely that of the observer itself. Fig. 5 shows the time-domain behavior at SCR 1.5, LL, the case with the largest true $|V_{\mathrm{neg}}|$.

Rotor-angle deviation. The deviation is set by fault type and SCR (10.7° to 135.0° for DSOGI-FLL, from SLG at SCR 5 to three-phase at SCR 1.5), and the extractor changes it very little: DSOGI-FLL, DSC and the EKF agree within a median of 0.3° and at most 2.0° in each of the twelve SCR–fault cases. ST-SMO, at $k_{\mathrm{neg}} = 0.25$, departs from their mean by at most 2.5° in eleven cases and by +13.4° at SCR 1.5 LL (62.0° against 48.6°), a case not explained here. For the three smooth extractors the data therefore show no extraction-specific signature in the virtual angle.

Regulation accuracy and sequence-estimation error (Fig. 6 and Table III; ground-truth runs at $T_s = 50$ μs, 36 unbalanced and 12 three-phase). The error of the estimated negative-sequence magnitude relative to the reference has medians of 0.027 %, 0.17 %, 0.52 % and 1.1 % for DSOGI-FLL, the EKF, DSC and ST-SMO (overall range 0.0002–4.2 %), the angle error medians of 1.0°, 3.3°, 5.2° and 14° (0.66°–25°), and the extraction-induced regulation error of the current reference, taken as the vector error (size and angle together) against the current commanded from the true voltage, medians of 2.9 %, 9.1 %, 14 % and 33 % (1.8–48 %). The order DSOGI-FLL, EKF, DSC, ST-SMO holds in all nine unbalanced cases for the angle error and for the vector error; the angle part of the latter equals the estimation angle error because the law is a pure rotation. DSC has a 0.52 % magnitude error but a 5.2° angle error, consistent with unfiltered harmonic content perturbing the phase more than the mean magnitude. Under three-phase faults the leakage of the estimate is $(0.4\text{–}1.2)\times10^{-6}$ pu for DSC, $(0.8\text{–}1.3)\times10^{-4}$ pu for DSOGI-FLL, $(0.6\text{–}1.2)\times10^{-4}$ pu for the EKF and 0.018–0.033 pu for ST-SMO. The static block counts are 60 for DSOGI-FLL, 40 for DSC, 54 for the EKF and 51 for ST-SMO, a coarse proxy for implementation effort and not a measurement of execution time.

TABLE II
SUMMARY OF THE METHOD COMPARISON AT THE FINAL DESIGN: MEDIANS OVER THE NINE UNBALANCED SCR–FAULT CASES (SLG, LL, LLG AT SCR 1.5, 3, 5); ALL METRICS AT $T_s = 50$ μs; ST-SMO AT $k_{\mathrm{neg}} = 0.25$ WITH A NEARLY INACTIVE INJECTION.

	DSOGI-FLL	DSC	EKF	ST-SMO
Settling time (ms)	258	23	24	1801
$\lvert V_{\mathrm{neg}}\rvert$ ripple (pu)	0.0032	0.0161	0.0101	0.0429
$\lvert V_{\mathrm{pos}}\rvert$ ripple (pu)	0.0053	0.0056	0.0173	0.0244
Rotor deviation, SCR 1.5 LL (°)	48.8	47.9	49.1	62.0
Estimate angle error (°)	1.0	5.2	3.3	14
Estimate magnitude error (%)	0.027	0.52	0.17	1.1
Regulation error, vector (%)	2.9	14	9.1	33
Recovery $\leq$ 1.2 s, primary / backup (of 12)	7 / 6	7 / 6	7 / 6	7 / 6
Static block count	60	40	54	51

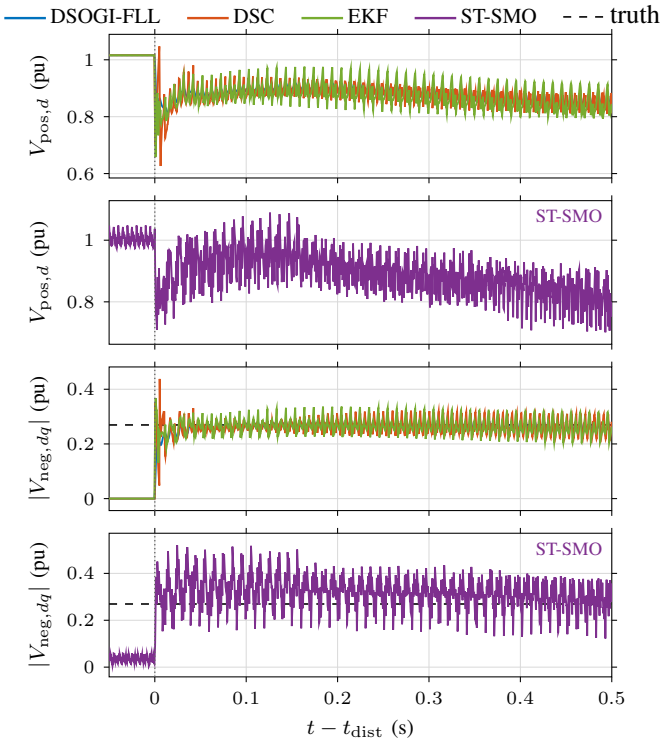


Fig. 5. Time-domain positive-sequence d-axis voltage and $|V_{\mathrm{neg},dq}|$ for the four extraction methods at SCR = 1.5, permanent LL fault, with ST-SMO on its own panels and the offline ground-truth $|V_{\mathrm{neg}}|$ of each run dashed (a constant, since the true $|V_{\mathrm{neg}}|$ is time-invariant over the settled window).

C. Active-Power Recovery Against IEEE 2800-2022 Clause 7.2.2.6

Over the whole sweep the recovery times of the three smooth methods differ by a median of 0.014 s and at most 0.23 s (SCR 5 LLG, 0.35 s clearing); the larger spreads occur at SCR 5. Recovery is therefore set by the VSM, the fault type and the SCR and not by the extractor (Fig. 7). At the

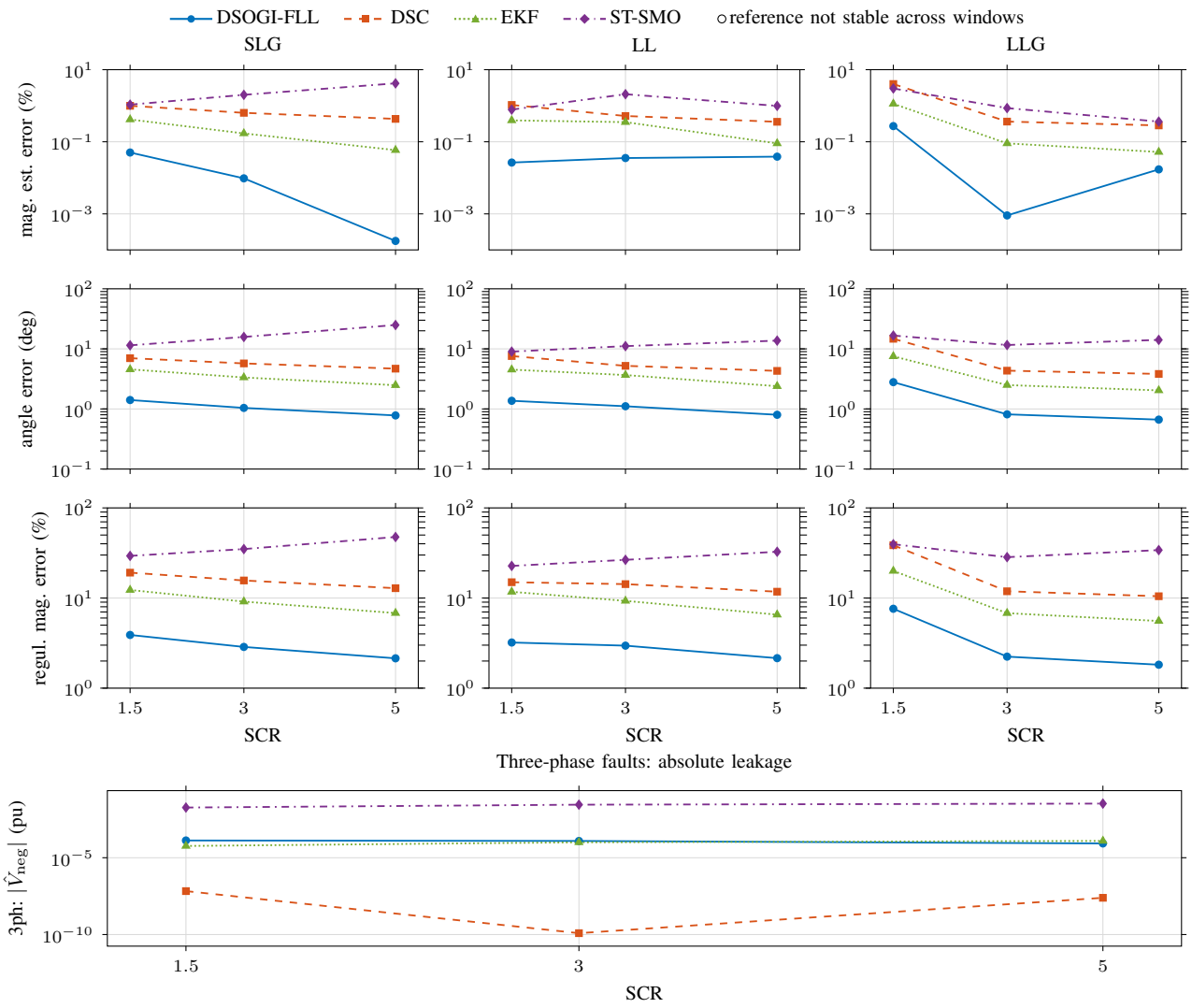


Fig. 6. Sequence-estimation magnitude error (row 1), angle error (row 2; identical for the controller's current reference, because the law is a pure rotation) and extraction-induced regulation error of the current reference, size and angle together (row 3) against the offline ground truth (50 μs runs), by SCR and extraction method, on logarithmic axes. Row 4: absolute leakage of the negative-sequence estimate under three-phase faults, where the true negative-sequence voltage is approximately zero.

TABLE III
SEQUENCE-ESTIMATION ANGLE ERROR AND EXTRACTION-INDUCED REGULATION ERROR (VECTOR, SIZE AND ANGLE TOGETHER) AGAINST THE OFFLINE GROUND TRUTH, BY SCR AND FAULT TYPE; PERMANENT UNBALANCED FAULTS, $T_s = 50$ μs. THE LAST ROW REPEATS THE MEDIANS OF TABLE II.

		Angle error (°)				Regulation error (%)			
SCR	Fault	DSOGI-FLL	DSC	EKF	ST-SMO	DSOGI-FLL	DSC	EKF	ST-SMO
1.5	SLG	1.41	7.00	4.56	11.5	3.89	19.1	12.3	29.3
1.5	LL	1.37	7.60	4.52	9.01	3.21	15.0	11.7	22.7
1.5	LLG	2.79	14.7	7.52	16.7	7.60	38.5	20.0	39.5
3	SLG	1.04	5.73	3.34	15.8	2.87	15.7	9.13	34.9
3	LL	1.11	5.22	3.67	11.1	2.96	14.3	9.30	26.5
3	LLG	0.81	4.34	2.50	11.6	2.24	11.9	6.80	28.4
5	SLG	0.78	4.69	2.48	25.0	2.14	12.9	6.81	47.5
5	LL	0.80	4.30	2.39	13.7	2.15	11.8	6.54	32.6
5	LLG	0.66	3.83	2.04	14.1	1.82	10.5	5.56	34.0
Median		1.04	5.22	3.34	13.7	2.87	14.3	9.13	32.6

1.2 s tolerance 28 of the 48 primary-clearing and 24 of the 48 backup-clearing combinations recover in time, 7 and 6 for each method. Primary clearing passes for SLG at all three SCR and for LL and LLG at SCR 1.5 and 3 (0.49–0.95 s), and fails for three-phase faults and for LL and LLG at SCR 5 (1.20–1.49 s). Backup clearing passes at SCR 3 for all faults

(1.12–1.17 s for LL and LLG, 1.197–1.199 s for three-phase) and for SLG and three-phase faults at SCR 5, and fails at SCR 1.5 for all faults (1.28–2.08 s) and for LL and LLG at SCR 5 (1.26–1.51 s). The classification is fragile: of the 72 runs of the smooth methods, 30 recover within 1.0 s, 9 between 1.0 and 1.2 s, 8 between 1.2 and 1.3 s and 25 later, and eight of the 96 recovery times lie within 0.03 s of the limit, all of them three-phase faults at SCR 3; at the 1.0 s target only 12 of the 48 backup combinations would pass, against all 28 primary ones.

ST-SMO at $k_{\mathrm{neg}} = 0.25$ recovers in all 24 temporary-fault runs and differs from the mean of the smooth methods by at most 0.09 s in all but one case. The exception is SCR 3 LL with 0.10 s clearing (0.90 against 0.49–0.50 s), which is consistent with the injection shortening recovery there; this was not isolated, because the extractor differs as well. At $k_{\mathrm{neg}} = 2$ ST-SMO did not recover in most runs because of the oscillation of Section V-D.

D. ST-SMO in the Closed Loop

After a temporary fault the loop formed by the ST-SMO estimate, the injection, the plant and the ST-SMO sustains an oscillation at $k_{\mathrm{neg}} = 2$, $\varphi_c = -13°$: the tail of $|V_{\mathrm{neg}}|$ is 0.395 pu (SCR 1.5 LL) and 0.301 pu (SCR 3 SLG), against 0.025 and 0.024 pu with the injection off. The cause is the injection loop gain and not the observer alone: the oscillation is not removed by the rate limit or by scaling the observer gains, and raising the gate thresholds removes it only by disabling the injection below $|V_{\mathrm{neg}}| \approx 0.3$ pu.

A map over the gain $k_{\mathrm{neg}} \in \{0.5, 1, 2\}$ and the commanded rotation $\varphi_c \in \{-60°, \ldots, +180°\}$ (nine angles) at SCR 3, SLG shows a stable post-clearing tail ($|V_{\mathrm{neg}}|$ near its own leakage of 0.0236 pu) only at $k_{\mathrm{neg}} = 0.5$ (five angles) and at $k_{\mathrm{neg}} = 1$, $\varphi_c = 180°$, and in no cell at $k_{\mathrm{neg}} = 2$. The two cells whose realized lead is near the band both oscillate (tails 0.23 and 0.26 pu), and every stable cell has its lead outside the band ($-163°$ to $-146°$, or $+148°$), so for ST-SMO the stable region and the compliant region do not overlap on this grid. The lower gain $k_{\mathrm{neg}} = 0.25$ is therefore adopted, at the price of an inactive injection.

Two further tests scope this result. Repeating the cells at $T_s = 100$, 50 and 25 μs does not remove the oscillation (tail 0.301, 0.298 and 0.306 pu at SCR 3 SLG), whereas at $k_{\mathrm{neg}} = 0.25$ the tail stays at 0.024–0.036 pu, so it is not a discretization artefact. The same map for DSC is stable in 24 of 27 cells, the exceptions being $k_{\mathrm{neg}} = 2$ with $\varphi_c = +60°$ to $+120°$, so a combination of gain and rotation can destabilize the loop in DSC as well; the contrast is that DSC has stable cells with the lead in the band ($k_{\mathrm{neg}} = 1$, $\varphi_c = 0°$: 98.8°, realized $|Y| = |I_{\mathrm{neg}}|/|V_{\mathrm{neg}}| = 0.59$) and ST-SMO has none. The usable gain of ST-SMO is thus limited by the closed-loop behavior of its estimate, with chatter the likely but untested cause. Both maps cover one operating point.

VI. Discussion

A. What Parameters the Extractor does not Influence

For the three smooth extractors, recovery time and rotor-angle deviation are set by the VSM, the fault type and the SCR: the extractor changes the recovery time by a median of 0.014 s and the rotor angle by at most 2.0°. The extractor matters through the noise and phase of its output. The methods order the same way, DSOGI-FLL, EKF, DSC, ST-SMO from best to worst, on the estimation errors, the regulation error of the current reference and the ripple of $|V_{\mathrm{neg}}|$ (Table II); the exceptions are settling time, where DSC and the EKF are fastest, and the ripple of $|V_{\mathrm{pos}}|$, where DSC beats the EKF. The choice of extractor is thus a choice about the noise margin and phase accuracy of the injection loop more than about the speed of the estimate. ST-SMO is compared at a gain at which its injection is nearly inactive.

The two frequency-adaptive methods are the two best, but the data do not attribute this to frequency adaptation. In the settled window the fitted frequency is within 0.017 Hz of 50 Hz, for which a fixed quarter-period delay causes an angle error of only about $0.03°$, against the $5.2°$ of DSC; the adaptive EKF is 3.2 times worse than the adaptive DSOGI-FLL; and the harmonic case separates the methods by their treatment of non-fundamental content. Frequency excursions during the transient are not resolved by settled-window metrics, so an advantage there is not excluded, and the relative advantage does not grow at low SCR (the DSC to DSOGI-FLL angle-error ratio is 5.0–5.6, 4.7–5.5 and 5.4–6.0 at SCR 1.5, 3 and 5).

Clause 7.2.2.6 recovery is governed by fault type and grid strength: each method passes 7 of the 12 primary and 6 of the 12 backup combinations, the passes being the same for all four except for marginal cases near 1.2 s. The one visible dependence on the injection is SCR 3 LL with 0.10 s clearing, where ST-SMO, whose injection is nearly inactive, is 0.4 s slower, although the extractor differs as well and the cause was not isolated. On cost, the most accurate method, DSOGI-FLL, has the highest block count (60), and the cheapest, DSC (40), has about five times its angle error under the harmonic content of the plant. Awal *et al.* find that a delay-based extractor does not limit the achievable current-control bandwidth, whereas a filter-based one does [7]; their criterion is small-signal stability and the criterion here is estimation accuracy and ripple, so the two results do not conflict. Within this plant and tuning, DSOGI-FLL gives the best extraction quality at an acceptable cost, and ST-SMO does not support the injection at the gain required for a realized lead in the band.

B. Commanded Versus Realized Current

Phase error is the critical quantity because the standard constrains it tightly: an extractor whose output lags the true vector by a time τ rotates the commanded current by $\omega\tau$, and at 50 Hz one millisecond is about $18°$, more than the $10°$ width of the lead window. The offline reference assumes that the settled voltage is a positive- and a negative-sequence fundamental pair, which is tested by the stability of the reference across analysis windows, and it says nothing about the interval just after the disturbance.

C. Limitations and Future Work

The study is simulation-only and uses one VSM architecture with a minimal damping retuning, so the ranking may not

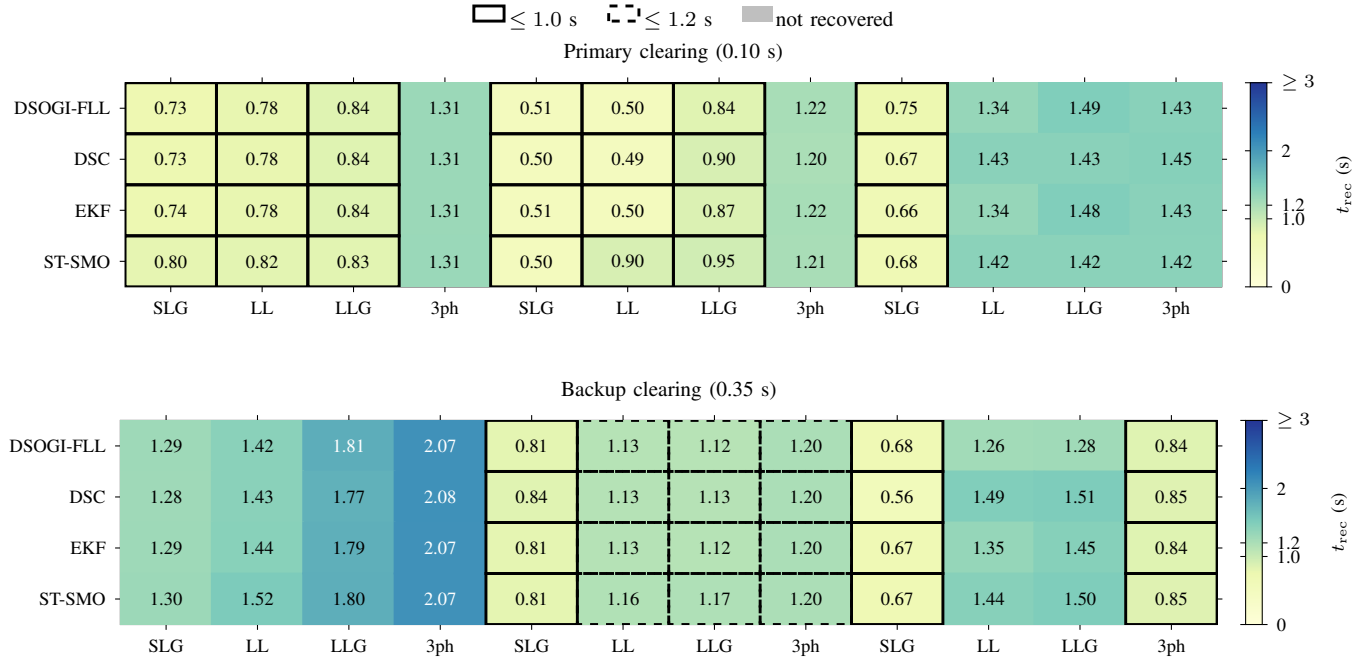


Fig. 7. Clause 7.2.2.6 recovery time across method, SCR, fault type and clearing duration, shown as a continuous colour scale with the 1.0 s and 1.2 s thresholds marked.

carry over to other GFM structures. The extractor gains were set from the literature or stated rules and not optimized per method, and the injection angle is an empirical calibration for this plant. The fault matrix uses one fault location and one X/R ratio, and the recovery classification depends on a power band chosen here and is fragile near 1.2 s. The extractor metrics depend on the step (the DSC angle error is 7.3° at 100 μs and 5.2° at 50 μs) although the ranking does not, and the ground-truth reconstruction was not repeated at 25 μs (Section IV-D). The origin of the 150 Hz and kHz content generated by the injection was not identified (Section IV-C). SCR $= 10$ is not covered, and no small-signal analysis of the injection loop exists.

Hardware-in-the-loop validation is the most direct extension. The SCR $= 10$ limit cycle calls for a linearized analysis of the active-power loop, the ST-SMO result for a boundary-layer saturation or an output filter, and the comparison can be widened to the decoupled double synchronous reference frame [5], a frequency-adaptive DSC and other current-limiting strategies [3].

VII. Conclusion

The paper compared DSOGI-FLL, DSC, the EKF and ST-SMO behind an identical interface in a full-order VSM grid-forming inverter, at SCR of 1.5, 3 and 5, for four fault types and three fault profiles, at a converged step of 50 μs.

DSOGI-FLL gives the smallest extraction error (median angle error 1.0° against 3.3°, 5.2° and 14° for the EKF, DSC and ST-SMO) and the lowest ripple, at the highest block count (60 against 40–54). DSC is the cheapest and exact on clean nominal-frequency signals, but it passes harmonics unfiltered. ST-SMO oscillates in closed loop at the gain used for the other methods and is run at a lower gain with a nearly inactive injection. Clause 7.2.2.6 recovery (28 of 48 primary and 24 of 48 backup combinations within 1.2 s) is set by fault type and grid strength, and the three smooth extractors differ in recovery time by a median of 0.014 s.

The commanded lead of the current reference does not determine the realized lead, so compliance must be assessed on the realized current; with a corrected rotation and rate limit the required lead is realized in 24 of 27 smooth-extractor cases. The default VSM tuning is unstable at SCR ≥ 5 regardless of the extractor and needed a damping retuning, and SCR 10 shows a method-independent limit cycle of the base model. The two-sequence power identity fails at the final gain because the injection adds third-harmonic content, and holds in all 36 runs once that content is included. The 100 μs step first used was not converged for LL and LLG at SCR 3, so the results are from 50 μs.

Acknowledgment

The author used Consensus, an AI-powered academic search tool, for literature search. The author used Claude (Anthropic) for LaTeX formatting, which the author reviewed and revised. The study design, the simulation model, all simulations and the interpretation of the results are the author's own. The author has read all cited sources and reviewed all text, numbers and figures.

References

[1] *IEEE Standard for Interconnection and Interoperability of Inverter-Based Resources (IBRs) Interconnecting with Associated Transmission Electric Power Systems*, IEEE Std 2800-2022, Apr. 2022, doi: 10.1109/IEEESTD.2022.9762253.

[2] M.-A. Nasr and A. Hooshyar, "Controlling grid-forming inverters to meet the negative-sequence current requirements of the IEEE Standard 2800-2022," *IEEE Trans. Power Del.*, vol. 38, no. 4, pp. 2541–2555, Aug. 2023, doi: 10.1109/TPWRD.2023.3246719.

[3] N. Baeckeland, D. Chatterjee, M. Lu, B. Johnson, and G.-S. Seo, "Overcurrent limiting in grid-forming inverters: A comprehensive review and discussion," *IEEE Trans. Power Electron.*, vol. 39, no. 11, pp. 14493–14517, Nov. 2024, doi: 10.1109/TPEL.2024.3430316.

[4] D. B. Rathnayake *et al.*, "Grid forming inverter modeling, control, and applications," *IEEE Access*, vol. 9, pp. 114781–114807, 2021, doi: 10.1109/ACCESS.2021.3104617.

[5] X. Zhao, X. Kestelyn, and D. Flynn, "A fault ride-through strategy for grid-forming converters under symmetrical and asymmetrical grid faults," *Elect. Power Syst. Res.*, vol. 235, Art. no. 110672, Oct. 2024, doi: 10.1016/j.epsr.2024.110672.

[6] M. A. Awal, M. R. K. Rachi, H. Yu, S. Schröder, and I. Husain, "Symmetrical components extraction for grid-forming voltage source converters," in *Proc. IEEE Energy Convers. Congr. Expo. (ECCE)*, Oct. 2022, pp. 1–8.

[7] M. A. Awal *et al.*, "Modeling, analysis, and design for small-signal stability in sequence-decomposed grid-forming control," *IEEE Trans. Ind. Appl.*, vol. 60, no. 1, pp. 865–875, Jan.–Feb. 2024, doi: 10.1109/TIA.2023.3326423.

[8] North American Electric Reliability Corporation (NERC), "Integrating inverter-based resources into low short circuit strength systems," Reliability Guideline, Dec. 2017.

[9] Q.-C. Zhong and G. Weiss, "Synchronverters: Inverters that mimic synchronous generators," *IEEE Trans. Ind. Electron.*, vol. 58, no. 4, pp. 1259–1267, Apr. 2011.

[10] S. D'Arco and J. A. Suul, "Virtual synchronous machines – Classification of implementations and analysis of equivalence to droop controllers for microgrids," in *Proc. IEEE PowerTech*, Grenoble, France, 2013.

[11] P. Kundur, N. J. Balu, and M. G. Lauby, *Power System Stability and Control*. New York, NY, USA: McGraw-Hill, 1994.

[12] A. D. Paquette and D. M. Divan, "Virtual impedance current limiting for inverters in microgrids with synchronous generators," *IEEE Trans. Ind. Appl.*, vol. 51, no. 2, pp. 1630–1638, Mar.–Apr. 2015, doi: 10.1109/TIA.2014.2345877.

[13] C. L. Fortescue, "Method of symmetrical co-ordinates applied to the solution of polyphase networks," *Trans. AIEE*, vol. 37, pt. II, pp. 1027–1140, 1918.

[14] E. Clarke, *Circuit Analysis of A-C Power Systems, Vol. I: Symmetrical and Related Components*. New York, NY, USA: Wiley, 1943.

[15] R. H. Park, "Two-reaction theory of synchronous machines – Generalized method of analysis – Part I," *Trans. AIEE*, vol. 48, pp. 716–727, 1929.

[16] S. Golestan, J. M. Guerrero, and J. C. Vasquez, "Three-phase PLLs: A review of recent advances," *IEEE Trans. Power Electron.*, vol. 32, no. 3, pp. 1894–1907, Mar. 2017.

[17] P. Rodríguez, A. Luna, M. Ciobotaru, R. Teodorescu, and F. Blaabjerg, "Advanced grid synchronization system for power converters under unbalanced and distorted operating conditions," in *Proc. 32nd Annu. Conf. IEEE Ind. Electron. (IECON)*, Paris, France, Nov. 2006, pp. 5173–5178, doi: 10.1109/IECON.2006.347807.

[18] J. Svensson, M. Bongiorno, and A. Sannino, "Practical implementation of delayed signal cancellation method for phase-sequence separation," *IEEE Trans. Power Del.*, vol. 22, no. 1, pp. 18–26, Jan. 2007, doi: 10.1109/TPWRD.2006.881469.

[19] M. Sun and Z. Sahinoglu, "Extended Kalman filter based grid synchronization in the presence of voltage unbalance for smart grid," in *Proc. IEEE PES Innov. Smart Grid Technol. Conf. (ISGT)*, Jan. 2011, pp. 1–4.

[20] R. Pérez-Ibacache, R. Carvajal, R. Herrera-Hernández, J. C. Agüero, and C. A. Silva, "A complex-valued stationary Kalman filter for positive and negative sequence estimation in DER systems," *Mathematics*, vol. 12, no. 12, Art. no. 1899, 2024, doi: 10.3390/math12121899.

[21] A. Levant, "Sliding order and sliding accuracy in sliding mode control," *Int. J. Control*, vol. 58, no. 6, pp. 1247–1263, 1993.

[22] P. J. Roache, *Verification and Validation in Computational Science and Engineering*. Albuquerque, NM, USA: Hermosa Publishers, 1998.

[23] M. H. J. Bollen, *Understanding Power Quality Problems: Voltage Sags and Interruptions*. New York, NY, USA: IEEE Press, 2000.

[24] R. Teodorescu, M. Liserre, and P. Rodríguez, *Grid Converters for Photovoltaic and Wind Power Systems*. Chichester, U.K.: Wiley, 2011.